Climate
of the Past

Rapid topographic growth of Diancang Shan, southeastern margin of the Tibetan Plateau, since 5.0–3.5 Ma

Chunxia Zhang[1,2], **Haibin Wu**[1,3], **Xiuli Zhao**[2], **Yunkai Deng**[1,3], **Yunxia Jia**[4], **Wenchao Zhang**[1], **Shihu Li**[5], and **Chenglong Deng**[3,5]

[1]Key Laboratory of Cenozoic Geology and Environment, Institute of Geology and Geophysics,
Chinese Academy of Sciences, Beijing 100029, China
[2]College of Earth Science and Engineering, Shandong University of Science and Technology,
Qingdao 266590, Shandong Province, China
[3]College of Earth and Planetary Sciences, University of Chinese Academy of Sciences, Beijing, China
[4]School of Geographical Science, Shanxi Normal University, Taiyuan 030031, China
[5]State Key Laboratory of Lithospheric Evolution, Institute of Geology and Geophysics,
Chinese Academy of Sciences, Beijing 100029, China

Correspondence: Chunxia Zhang (cxzhang@mail.iggcas.ac.cn)

Abstract. As a crucial geological, climatic, and ecological boundary in the southeastern margin of the Tibetan Plateau (SEMTP), the topographic evolution of Diancang Shan (DCS) remains unclear due to the lack of direct constraints on its paleoelevation. Here, we quantitatively reconstructed changes in annual mean temperature (ANNT) based on palynological data from the terrestrial Dasongping section ($\sim$ 7.6–1.8 Ma) in the Dali Basin, located at the northeastern margin of DCS in Yunnan, China. Integrating the thermochronological data from the eastern and southern margins of DCS, we have clarified the paleotopographic evolution of DCS during this period: the paleoelevation of DCS likely exceeded 2000 m a.s.l. (above sea level) due to initial normal faulting at $\sim$ 7.6 Ma, possibly comparable to the current average elevation ($\sim$ 2200 m a.s.l.) of the surrounding Dali Basin region. Significant growth occurred between $\sim$ 5.0 and $\sim$ 3.5 Ma, with at least $\sim$ 1000 m uplift gain in the northern segment and up to $\sim$ 2000 m in the southern segment of DCS, caused by the intensification of normal faulting activities. Finally, the northern segment of DCS reached the elevation of $\sim$ 3500 m a.s.l. after $\sim$ 1.8 Ma. Our findings suggest that the quantitative ANNT reconstruction, combined with thermochronological and sedimentary data, can significantly improve constraint on the paleotopographic evolution of DCS.

1 Introduction

The southeastern margin of the Tibetan Plateau (SEMTP) has evolved tectonically as an important accommodation zone during the post-collisional intracontinental deformation between the Indian and Eurasian continents (Tapponnier et al., 1990; Houseman and England, 1993; Leloup et al., 1995; Clark and Royden, 2000; Clark et al., 2004, 2005). Much of the intracontinental deformation of the SEMTP during the Cenozoic has been accommodated by strike-slip fault systems, of which the Ailao Shan–Red River shear zone (ASRRSZ) (Fig. 1a) is the largest one (Harrison et al., 1995; Leloup et al., 1993, 1995; Tapponnier et al., 1990; Wang et al., 1998, 2006). The last transformation of shear zone with dextral ductile-to-brittle transitional normal faulting in the Late Cenozoic was thought to have resulted in large-scale uplift and erosion, leading to the formation of today's mountains within the ASRRSZ (Allen et al., 1984; Tapponnier et al., 1990; Leloup et al., 1993, 1995; Wang et al., 1998, 2006). Diancang Shan (DCS), lying in the northwestern part of the ASRRSZ in the SEMTP (Fig. 1a), is a transition belt of the high Tibetan Plateau to the low relief of eastern and southern Asia and a neighboring belt of subtropics to the east and middle subtropics to the west. As a significant geological, climatic, and ecological boundary within the SEMTP,

the tectonic evolution of DCS provides great information on our understanding of the uplift process of the Tibetan Plateau (Tapponnier et al., 1990; Leloup et al., 1993; Harrison et al., 1995; Wang et al., 1998, 2006, 2020a, b, 2022).

Clarifying the paleoelevation changes of DCS is important for comprehending both the tectonics and the climatic effects in this unique geographical location. Most thermochronological studies primarily focused on tectonic activities surrounding the DCS range, revealing that the extensive right-lateral strike-slip movement in this region experienced numerous episodes of obvious shear displacement at ~ 8.0, ~ 5.0, 2.7, and 2.1 Ma, respectively (Leloup et al., 1993; Harrison et al., 1995; Fan et al., 2006; Xiang et al., 2007; Cao et al., 2011; Han et al., 2011; Li et al., 2012). Only very few thermochronological studies mentioned that DCS had reached its maximum elevation at ~ 4.7 Ma, followed by significant unroofing during the Quaternary (Leloup et al., 1993). However, the existence of relict surface on the top of DCS indicates that there was no unroofing during the Late Cenozoic. Wang et al. (2006) suggested that the rock-cooling events around DCS revealed by low-temperature thermochronological data were not caused by unroofing but possibly resulted from normal faulting along the mountain front. Schildgen et al. (2018) proposed that regional variations in exhumation rates can be accurately assessed by integrating local findings that encompass thermochronological data and location-specific information. Although numerous geochronological and thermochronological data exist, documenting multiple episodes of tectonic activities around the DCS range, there is currently a significant lack of precise constraints on the paleoelevation of DCS throughout the period since the Late Cenozoic.

The coupling between sedimentary basins and orogenic belts is an important geomorphic evolutionary process. The Sanying Formation is widely distributed along piedmont and hill-front areas and in fault-controlled basins in Yunnan, southwestern China, and has been used to constrain the reactivation of the sinistral Dali fault system and the timing of surface uplift of the SEMTP (Wang et al., 1998; Clark et al., 2005). The Sanying Formation spans the interval from the Late Miocene to the Early Pleistocene (~ 7.6–1.8 Ma) in the Dali Basin, which is the most complete fluviolacustrine sequence in the NE flank of Diancang Shan (DCS) (Li et al., 2013). The activity of the Dali fault system and the surface uplift of DCS during the late Neogene have been reconstructed and constrained using chemical compositions and bulk mineralogical characteristics of sedimentary rocks from the Dasongping section (C. X. Zhang et al., 2020). As mountain elevation has a direct impact on climate and vegetation, paleobotany recorded in a sedimentary basin can be utilized as a proxy for estimating paleoelevation. Pollen assemblages in sedimentary sequences have been used to reconstruct paleoelevation in the Tibetan Plateau (Song et al., 2010; Sun et al., 2014) and indicate the rise of the northeastern parts of Tibetan Plateau (Dupont-Nivet et al., 2008; Miao

et al., 2022). In this study, we investigate palynological data of the late Neogene sedimentary record from the Dasongping section and quantitatively reconstruct changes in the annual mean temperature (ANNT) based on pollen data. By combing the ANNT with the sediment accumulation rate (SAR) of the Dasongping section and thermochronological data from the eastern and southern margins of DCS, we aim to quantitatively reconstruct the paleoelevation evolution of DCS during the Late Cenozoic.

2 Materials and methods

2.1 Geological setting and sampling

The present landscape of DCS is an elongated metamorphic massif, with a length of 80 km and a width of ~ 50 km. It has an average elevation of 4000 m a.s.l. in the southern segment, 3700 m a.s.l. in the middle, and 3500 m a.s.l. in the northern segments, with the highest peak of 4122 m a.s.l. The top of DCS is a very flat relict surface which can be traced from the northern edge to the southern edge of the massif for 100 km (Wang et al., 1998; Fan et al., 2006). DCS is ~ 1800 m above the surrounding regions (average elevation ~ 2200 m a.s.l.), and exhibits vertical climatic zoning vegetation (Ming and Fang, 1982).

The eastern flank of DCS exhibits triangular facets separated by deep canyons (Wang et al., 2006), suggesting its normal faulting activity. The Dali Basin formed in response to movement on the east-dipping Erhai normal fault system, with an elevation of 1980 m a.s.l., which is a pull-apart basin located to the east of DCS (Fig. 1a). It includes the Eryuan Basin in the north and the Erhai Basin in the south (Fig. 1b). The total thickness of Neogene–Quaternary sediments in the Dali Basin is about 2200 m (Guo et al., 1984). These phenomena suggest that the eastern flank of DCS corresponds to an active east-dipping normal fault and that the thick sediments in the basin result from rapid erosion of uplifted DCS (Guo et al., 1984; Tapponnier et al., 1990; Leloup et al., 1993). The Dali Basin has a northern tropical monsoon climate, with a mean annual precipitation of 750 mm and a mean annual temperature of 13 °C (Chen, 2001).

The Dasongping section preserves the best exposures of Neogene coal-bearing sedimentary rocks of the Sanying Formation (Li et al., 2013) in the Eryuan Basin on the northern flank of DCS (Fig. 1b and d) at an elevation of 2174–2633 m a.s.l. The terrestrial record has a thickness of ~ 1000 m (Fig. 1d) and spans the interval from ~ 7.6 to ~ 1.8 Ma; it is disconformably overlapped by unconsolidated Quaternary conglomerates and is underlain by Silurian limestone (Li et al., 2013). Lithological variations allow five facies associations (FAs) to be identified from bottom to top: swamp/shore lake facies (FA1; 0–300 m), fluvial or lacustrine facies (FA2; 300–505 m), lacustrine with alluvial facies (FA3; 505–750 m), fluvial and alluvial facies (FA4; 750–965 m), and foothill–pluvial facies (FA5; 965–1000 m)
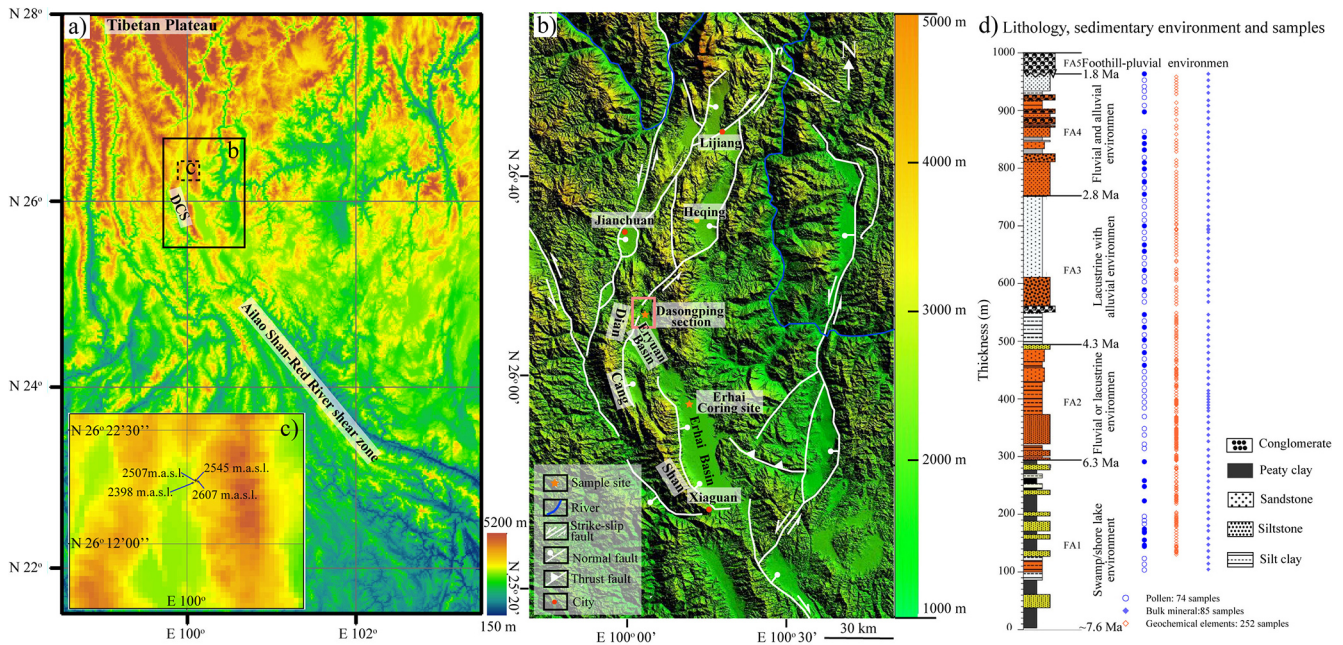
Figure 1. (a) Location of the study area. **(b)** Shaded relief map of the Dali highlands and the Dali fault system, as well as Diancang Shan. The distribution and configuration of active faults are modified after Wang et al. (1998). **(c)** The altitude distribution of the four surface samples. **(d)** Lithologies, sedimentary facies, and samples for pollen, bulk mineral, and geochemical analyses. DCS: Diancang Shan. Solid blue circles in panel **(d)** correspond to samples that yielded abundant pollen grains.

(Fig. 1d) (Li et al., 2013; C. X. Zhang et al., 2020). Bulk samples were collected from the mudstones, siltstones, and sandstones of the Dasongping section at an ~ 1 m interval. A total of 74 samples with an average sampling interval of ~ 10 m were analyzed for their palynological assemblages. Additionally, 4 surface samples within elevations of ~ 2400–2600 m from the Dasongping section area (Fig. 1c) were collected for their palynological analysis.

2.2 Methods

2.2.1 Pollen data and climate data

The 78 samples analyzed for pollen were treated with HCl (15 %) and NaOH (~ 3 %) to remove carbonate and organic matter, respectively. Pollen in each sample was concentrated using heavy-liquid separation with ZnI_2. Before mounting the palynomorphs in glycerin jelly, HF (40 %) and HCl (36 %–38 %) were used to remove silicates. Finally, 31 out of the 74 samples and 4 surface samples with an average elevation of 2500 m a.s.l. (Fig. 1c) yielded abundant pollen grains, while very few pollen grains (< 5 grains) or none were obtained from sandstone, silty sandstone, and red siltstone (Fig. 1d, Table S1 in the Supplement). Excluding aquatic taxa, pteridophytes and Cyperaceae, a minimum of 270 grains were counted per sample, and more than 300 pollen grains were counted for 25 samples (Fig. 2, Table S1). We calculated the pollen and spore percentages of each taxon base relative to the sums of terrestrial pollen

grains and total grains, respectively. Palynological datasets of the late Holocene and mid-Holocene from the Erhai coring (Fig. 1b) were compiled from the literature (Shen et al., 2006), and all pollen sample preparation methods followed Liu et al. (1986).

We use the modern surface pollen assemblage data of China compiled by Sun et al. (2020). This dataset comprises 1630 sample sites, covering most of the regions of China. The modern climate data from the WorldClim 2.1 database (Fick and Hijmans, 2017) were obtained. The database provided gridded climate data at a spatial resolution of 30 s (~ 1 km^2) and was the average for the years 1970–2000.

2.2.2 Climate reconstruction

To reconstruct the history of vegetation evolution, we translated pollen assemblages into vegetation types using the biomization procedure proposed by Prentice et al. (1996). This method classifies individual pollen taxa into taxa plant functional types (PFTs) according to plant stature, leaf form, phenology, and climatic adaptations and then into vegetation types (biomes) defined by the dominant PFTs. In this study, we calculated biome scores and reconstructed vegetation changes using the latest PFT biome matrixes defined for the China region (Sun et al., 2020).

We used the PFT-based modern analogue technique (MAT) to quantitatively reconstruct the annual mean temperature (ANNT) following the procedure pro-
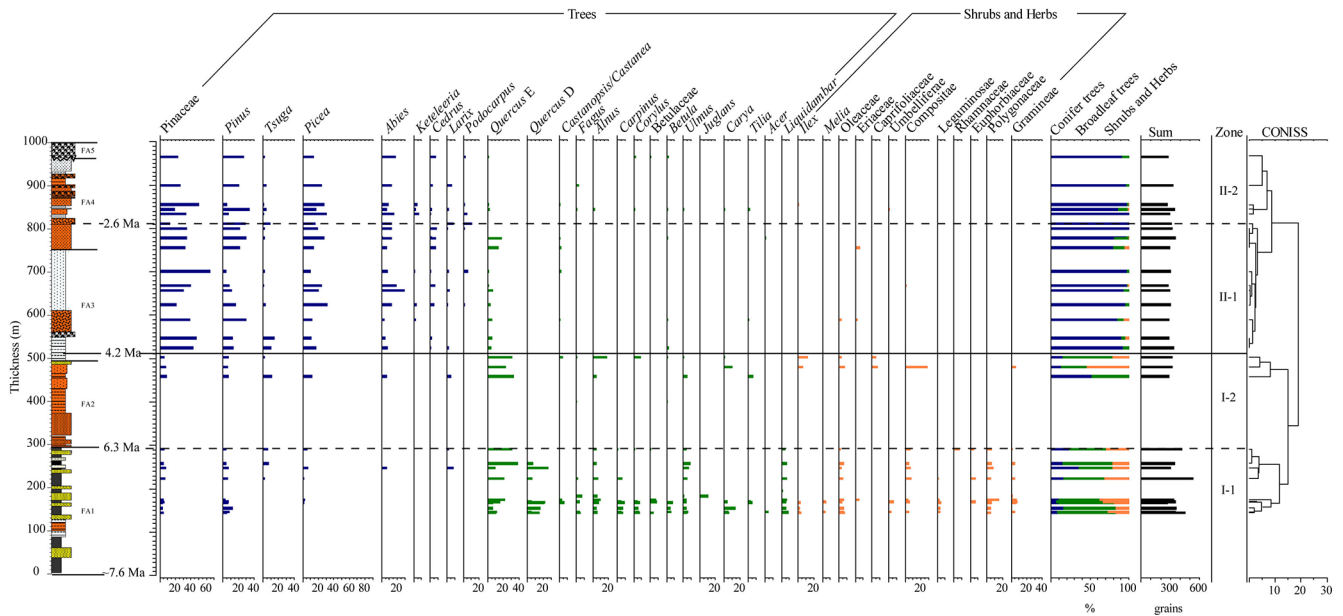
Figure 2. Variations in lithology, sedimentary facies, and pollen assemblages through the Dasongping section. Lithological captions are same as Fig. 1d.

posed by Zhang et al. (2022a). Briefly, the original taxa were converted into PFT scores. The modern analogues were identified using the squared chord distance metric of dissimilarity. The dissimilarity-weighted climate of the six closest modern analogues was assigned to the fossil sample. The performance of this model was evaluated using the bootstrap cross-validation. The performance of the weighted averaging partial least squares (WAPLS) model was also evaluated with the same calibration set for comparison. All the analyses were carried out using R software (version 4.3.3; R Core Team, 2024). The predicted ANNT based on PFT-based MAT showed a more significant linear relationship ($R^2 = 0.83$) with the observed ANNT than weighted averaging partial least squares (WAPLS; component $= 3$) ($R^2 = 0.80$) estimated by bootstrapping cross-validation (Fig. S1 in the Supplement). It is reasonable that the scatter plots of the PFT-based method exhibit higher dispersion than those of the WAPLS method because the modern analogues might be impacted by non-climatic factors (Zhang et al., 2022b).

2.2.3 Paleoelevation reconstruction

Pollen assemblages in the sedimentary section were the results of mixing at different elevations; the paleoclimate quantitative reconstruction based on the PFT-based MAT in the Dali Basin would be more sensitive to the variation in elevation. After excluding the influence of global temperature changes, the quantitative differences in ANNT values between surface samples at 2500 m a.s.l. and sedimentary records record the topographic variations of DCS. To reduce

the systematic error in estimating ancient elevations from pollen data, we employed the temperature mean anomaly, specifically quantifying the disparities in ANNT values between sedimentary archives and contemporary surface samples situated at 2500 m a.s.l., as a means to reconstruct the paleoelevation of DCS. The paleoelevation of DCS (in per Ma interval) was calculated, using the common temperature lapse rate (TLR) of 5–6 °C km^{-1} (Miao et al., 2022) , based on the following formula:

$$\text{elevation}_{\text{paleo}} = 2500 - 1000 \cdot (\text{ANNT}_{\text{mean-anom}}$$
$$-\, \text{SST}_{\text{mean-anom}})/\text{TLR}, \qquad (1)$$
$$\text{ANNT}_{\text{mean-anom}} = \text{ANNT}_{\text{mean}} - \text{ANNT}_{\text{mean@2500 m a.s.l.}}. \quad (2)$$

$\text{ANNT}_{\text{mean}}$ is the mean ANNT per Ma period of the Dasongping section, and $\text{SST}_{\text{mean-anom}}$ is the tropical sea surface temperature mean anomaly per Ma period. $\text{SST}_{\text{mean-anom}}$ data from the literature (Herbert et al., 2016; Holbourn et al., 2018) and $\text{ANNT}_{\text{mean-anom}}$ and $\text{SST}_{\text{mean-anom}}$ are shown in Fig. 6f.

2.2.4 Sediment accumulation rate and thermochronological data

Sediment accumulation rate (SAR) is an important proxy to reflect the intensity of sediment deposition in a basin, which is affected by sediment transport capacity, sediment source, and climate. Therefore, SAR is of great significance for understanding basin infilling processes, analyzing sedimentary histories, and studying geomorphic features. The 1000 m thick Dasongping section has been well constrained

from 7.6–1.8 Ma by magnetostratigraphic (Fig. 1d), which yields SARs varying in a range of 38.2–462.4 m Ma^{-1} (Li et al., 2013).

Low-temperature thermochronology is a valuable tool for reconstructing the paleotopography and the long-term exhumation history of orogenic mountain ranges (Reiners and Brandon, 2006; Herman et al., 2013). A total of 53 sets of thermochronological data from the eastern and southern margins of DCS were obtained from the previously published literature (Table S2). The existing thermochronological data per 0.5 Myr intervals were counted, and the frequency vs. age of all data from the eastern margin and the southern margin of DCS is shown in Fig. 5.

3 Results

3.1 Pollen assemblages

A total of 47 pollen and spore species were identified in 31 samples (Fig. 1d) from the Dasongping section. Gymnosperms (with a mean value of 64.1 %) and angiosperms (28.0 %) are dominant. The content of pteridophytes (including *Polypodium* L., *Pteris* L., *Araiostegia* Cop., *Leucostegia* Presl., *Hicriopteris* Presl., and *Selaginella*) is low (7.9 %), and their indication for the environment is not obvious, so pteridophytes are omitted from the spectrum. Conifer trees (mean value of 59.0 %) and broadleaf trees (18.4 %) are dominant, followed by shrubs and herbs (11.9 %) (Fig. 2). The dominant taxa are Pinaceae (20.9 %), *Pinus* (12.5 %), *Picea* (11.7 %), *Quercus* evergreen types (*Quercus*E) (10.6 %), and *Abies* (6.6 %). Pollens of *Tsuga*, *Keteleeria*, *Cedrus*, *Larix*, *Quercus* deciduous types (*Quercus*D), *Fagus*, *Betula*, *Alnus*, *Carpinus*, *Corylus*, *Ulmus*, *Liquidambar*, Oleaceae, Poaceae, Asteraceae, and Polygonaceae are common in all analyzed samples. Minor occurrences of Betulaceae, *Juglans*, *Carya*, *Tilia*, *Acer*, *Ilex*, Apiaceae, Ericaceae, *Melia*, Araliaceae, Fabaceae, Rhamnaceae, Euphorbiaceae, *Nitraria*, and Caprifoliaceae occur in some samples. Variations in the pollen percentages allow the pollen diagram to be divided into two main zones, Zone I (0–510 m, ∼ 7.6–4.2 Ma) and Zone II (510–1000 m, ∼ 4.2–1.8 Ma), and four subzones (Fig. 2).

In Zone I (14 samples, 0–510 m, ∼ 7.6–4.2 Ma), broad-leaved tree pollen (mean of 38.5 %) and shrubs and herbs (mean of 25.2 %) dominate the assemblage, followed by coniferous tree pollen (mean of 17.3 %). Broad-leaved tree pollen is a major group, including *Quercus*E (19.0 %); *Quercus*D (8.8 %); *Alnus* (5.8 %); *Ulmus* (3.7 %); *Liquidambar* (3.7 %); *Corylus* 3.5 %); *Carpinus* (3.2 %); *Carya* (3.1 %); and minor *Fagus*, *Castanopsis/Castanea*, *Castanea Mill.*, Betulaceae, *Betula*, *Juglans*, *Tilia*, and *Acer*. Herbaceous pollen is also present, including *Compositae* (5.2 %); *Oleaceae* (4.3 %); *Polygonaceae* (4.3 %); and minor *Ilex*, Fabaceae, Euphorbiaceae, and *Melia*. The dominant coniferous taxa include *Pinus* (6.1 %), Pinaceae (4.9 %), *Picea* (2.2 %), *Tsuga* (2.1 %), and minor *Abies* and *Larix*. Due

to unfavorable conditions for pollen conservation, no statistically sufficient pollen and spores were obtained from sandstone and silty sandstone during the period of ∼ 6.3–4.8 Ma. There is more broad-leaved tree pollen in Subzone I-1, whereas there is more coniferous pollen in Subzone I-2 (Fig. 2).

In Zone II (17 samples, 510–1000 m, ∼ 4.2–1.8 Ma), coniferous tree pollen (93.3 %) dominates the assemblages, followed by minor broad-leaved tree pollen (1.9 %) and shrubs and herbs (1.0 %). The dominant coniferous taxa include Pinaceae (34.0 %); *Picea* (19.5 %); *Pinus* (17.9 %); *Abies* (11.2 %); *Tsuga* (3.4 %); *Cedrus* (2.9 %); and minor *Keteleeria*, *Larix*, and *Podocarpus*. Broad-leaved tree pollens, including *Quercus*E (3.7 %) and minor *Castanopsis/-Castanea*, *Fagus*, *Alnus*, *Corylus*, Betulaceae, and *Betula*, are observed in only a few samples. Of note, there are more *Picea*, *Pinus*, *Keteleeria*, *Cedrus*, *Larix*, and *Podocarpus* in Subzone II-2 than in Subzone II-1 (Fig. 2).

Studies of four modern surface samples show that coniferous tree pollens (mainly *Pinus* (81.3 %–91.2 %), *Tsuga* (0.2 %–1.1 %), and *Abies* (0 %–1.6 %)) and fewer broad-leaved tree pollens (mainly *Alnus* (2.5 %–4.9 %), *Betula* (0 %–3.0 %), and *Corylus* (0 %–2.2 %)) are present within the elevations of 2400–2600 m a.s.l. from the Dasongping section. Pollen assemblages are consistent with the modern vegetation distributions, cultivated *Pinus* forests (2500–3000 m a.s.l.), on the eastern slope of DCS (Fig. 3).

3.2 Paleovegetation, ANNT, and paleoelevation

From bottom to top, the modern vegetation belts of DCS are as follows (Fig. 3): (1) cultivated *Pinus* forests (in the eastern DCS at altitudes of ∼ 2500–3000 m a.s.l.; in the western DCS at altitudes of ∼ 1750–2550 m a.s.l.); (2) middle subtropical broadleaf evergreen forest (MTFO) (east: absent; west: ∼ 2550–2900 m a.s.l.); (3) cool temperate mixed forest (COMX) (east: ∼ 3000–3350 m a.s.l.; west: ∼ 2900–3200 m a.s.l.); (4) *Tsuga dumosa*, broad-leaved forests, and cold evergreen conifer forest (CLEC) (east: ∼ 3350–3800 m a.s.l.; west: 3200–3700 m a.s.l.); and (5) *Abies delavayi*, tundra with Rhododendron thickets, and alpine meadow (ALME) (east: ∼ 3850–4112 m a.s.l.; west: ∼ 3700–4112 m a.s.l.). The very flat top of the DCS massif is covered by grasslands, shrubs, and ponds (Fan et al., 2006).

The dominant vegetation types are MTFO and WAMF (north subtropical mixed forest) during the period of ∼ 7.6–6.3 Ma and ∼ 4.8–4.2 Ma, respectively (Fig. 4a). COMX and CLEC are dominant during ∼ 4.2–1.8 Ma, with the exceptions of WAMF at ∼ 4.2–2.6 Ma (Fig. 4a). To the east of DCS, modern vegetation belts of MTFO, COMX, and CLEC are distributed at altitudes of ∼ 2500–3000, ∼ 3000–3350, and ∼ 3350–3850 m a.s.l., respectively (Fig. 3). These results indicate that the vegetation in the Dali Basin has been characterized by vertical zonation since the Pliocene. The ANNT values in the Dasongping section vary in the range of ∼ 3.9–
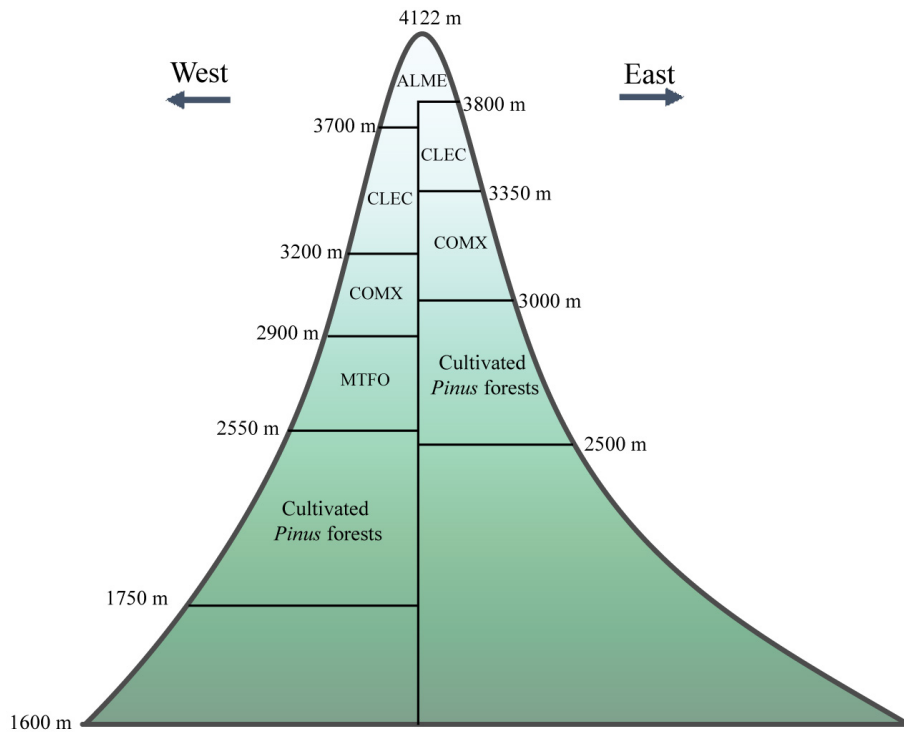
Figure 3. Vertical distribution of modern vegetation on Diancang Shang, simulated using the taxa–PFT–biomes matrixes defined for the China region (Sun et al., 2020). MTFO means middle subtropical broadleaf evergreen forest, COMX means cool temperate mixed forest, CLEC means cold evergreen conifer forest, and ALME means alpine meadow.

15.1 °C, and they have higher mean values of 11.6 °C in Zone I and lower mean values of 5.3 °C in Zone II (Fig. 4b). The mean ANNT values of zones I-1 ($\sim$ 7.6–6.3 Ma), I-2 ($\sim$ 6.3–4.2 Ma), II-1 ($\sim$ 4.2–2.6 Ma), and II-2 ($\sim$ 2.6–1.8 Ma) in the Dasongping section are 11.6 $\pm$ 2.3, 12.0 $\pm$ 5.1, 6.1 $\pm$ 2.0, and 4.6 $\pm$ 0.5 °C, respectively (Fig. 4b).

The ANNT of surface samples from 2400 to 2600 m a.s.l. and the ANNT of the late Holocene and mid-Holocene from Erhai coring (elevation of ca. 1974 m a.s.l.) (Shen et al., 2006) are reconstructed. The mean ANNT of surface samples is 7.9 $\pm$ 1.7 °C, which is lower than the modern ANNT ($\sim$ 12.0 °C) at 2500 m a.s.l. The mean ANNT of the late Holocene and mid-Holocene from Erhai coring is 11.8 $\pm$ 1.3 and 13.9 $\pm$ 1.0 °C, respectively; both are lower than the ANNT ($\sim$ 15.1 °C) at present o54n the lakeshore ($\sim$ 1970 m a.s.l.) (Shen et al., 2006). However, the ANNT in the mid-Holocene from Erhai is $\sim$ 2.1 °C higher than that in the late Holocene, which is consistent with the fact that the annual mean temperature during the Holocene optimum in southern China was generally 2–3 °C higher than it is now (Shen et al., 2006; Zhang et al., 2022a, b). This indicates that the relative changes in the reconstructed ANNT are reliable, even though the reconstructed ANNT may possibly be underestimated based on the pollen assemblage of mixed palynological spectra from different altitudes in mountain areas. To mitigate the bias in reconstructing paleoelevation using

the reconstructed ANNT directly, we utilized the temperature mean anomaly, which represents the quantitative differences in ANNT values between sedimentary records and surface samples located at 2500 m a.s.l., to reconstruct the paleoelevation of DCS. Based on Eqs. (1) and (2), our reconstruction inferred that the paleoelevation of DCS may be $\sim$ 2000–2200 m a.s.l. at $\sim$ 7.6–4.2 Ma and $\sim$ 3100–3350 m a.s.l. at $\sim$ 3.6–1.8 Ma. The above information implied that the northeastern segment of DCS may have risen by $\sim$ 1000 m at $\sim$ 4.2–3.6 Ma.

4   Discussion

4.1   Tectonic activities surrounding the DCS range during the Late Miocene to Pleistocene

The SEMTP may have undergone initial topographic uplift and widespread exhumation from the Eocene to the early Oligocene. The region situated north of 26° N has been at or close to its current elevation since $\sim$ 40 Ma (Hoke et al., 2014). Additionally, the Mangkang and Gonjo basins, located within the eastern Qiangtang terrane, were likely to have attained elevations of $\sim$ 2.5–3 km by the end of the Eocene (Su et al., 2019; Tang et al., 2017; S. H. Li et al., 2020). The Ailao Shan–Diancang Shan region underwent ductile deformation that began at no less than $\sim$ 34 Ma and
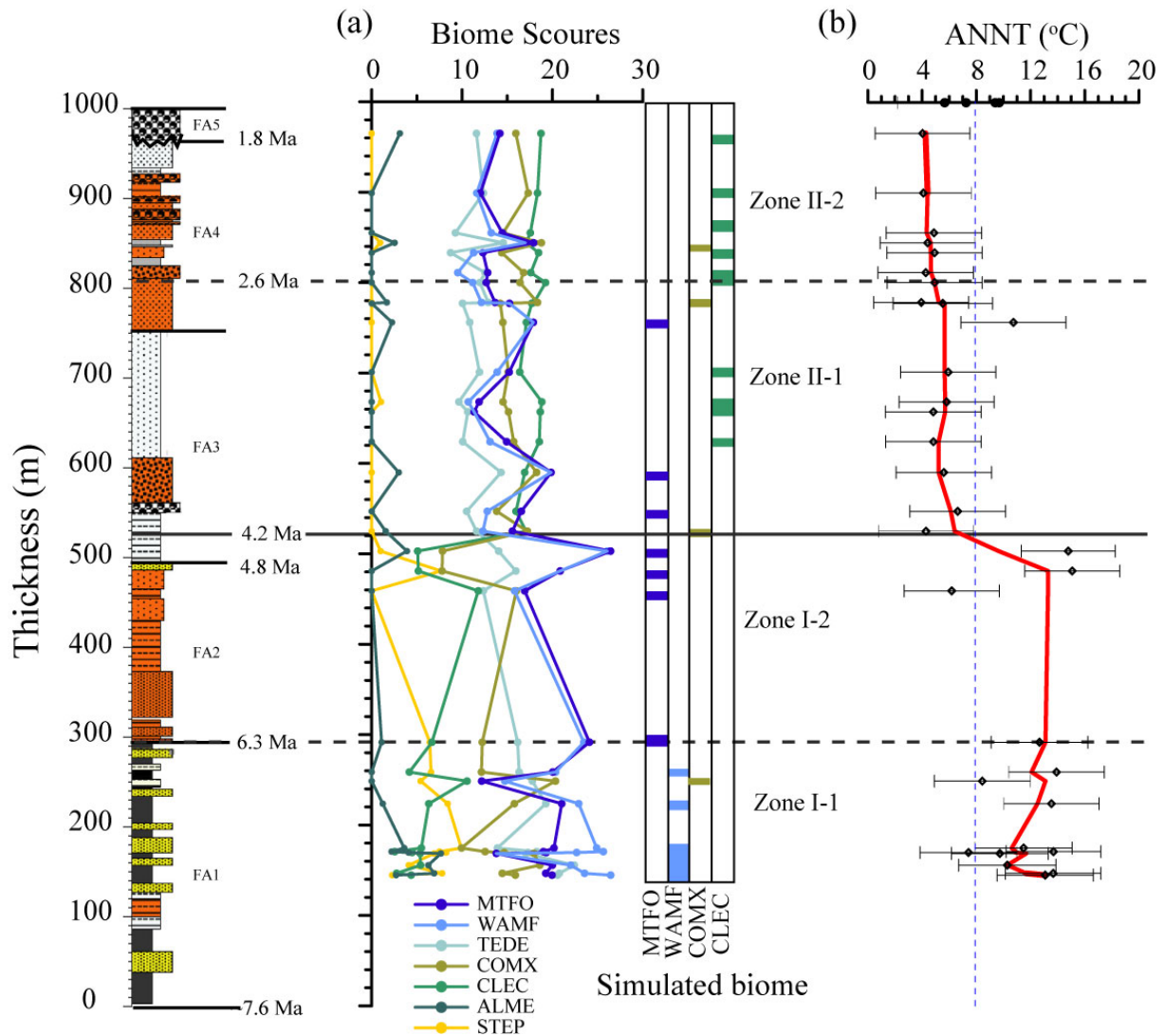
Figure 4. Variation in lithology and sedimentary facies. **(a)** Biome scores and simulated biome type. **(b)** ANNT of the Dasongping section.

terminated between 20 and 17 Ma. This deformation was characterized by large-scale differential uplift occurring concurrently with erosion, resulting in the erosion of the mountain range and the adjacent area into a landform with low relief (Tapponnier et al., 1990; Tang et al., 2013; Gourbet et al., 2017; Cao et al., 2021). During the Late Cenozoic period, the region experienced dextral ductile-to-brittle transitional normal faulting marked by regional uplift that was synchronous with the incision of river systems (Leloup et al., 1993, 1995; Wang et al., 1998, 2006, 2022). Based on the K-feldspar ^{40}Ar/^{39}Ar ages of dextral sheared mylonites, Leloup et at. (1993) proposed that the present topography of DCS was a consequence of normal faulting along the margin of the mountain, which was initiated at ~ 4.7 Ma. Geochronological data at different locations on DCS, including ^{40}Ar/^{39}Ar, K–Ar, and low-temperature thermochronological ages, show that the most recent phase of uplift of DCS ranged from

~ 5 to ~ 0 Ma (Cao et al., 2011; Fan et al., 2006; Han et al., 2011; Harrison et al., 1995; Leloup et al., 1993; Li et al., 2012).

The synthesis of existing thermochronological data from the eastern and southern margin of the DCS cluster occurs between ~ 7.0 and 3.5 Ma, with two high-frequency periods at ~ 6.5–5.5 and ~ 4.5–4.0 Ma, respectively (Fig. 5), which indicated that rock-cooling events occurred frequently, especially in the eastern margin of DCS during the period of ~ 4.5–4.0 Ma. The history of tectonic activities surrounding the DCS shear zone can be determined by using thermochronological data and the increase in SAR, the change in provenance, and the timing of conglomerate occurrence in the Neogene sediment sequence. The significant increases in SAR occurred at intervals of ~ 7.6–6.3, ~ 3.6–3.4, and ~ 2.7–1.8 Ma (Fig. 6b), which corresponded to the initial time of dextral normal faults at ~ 8 Ma reviewed by geochrono-
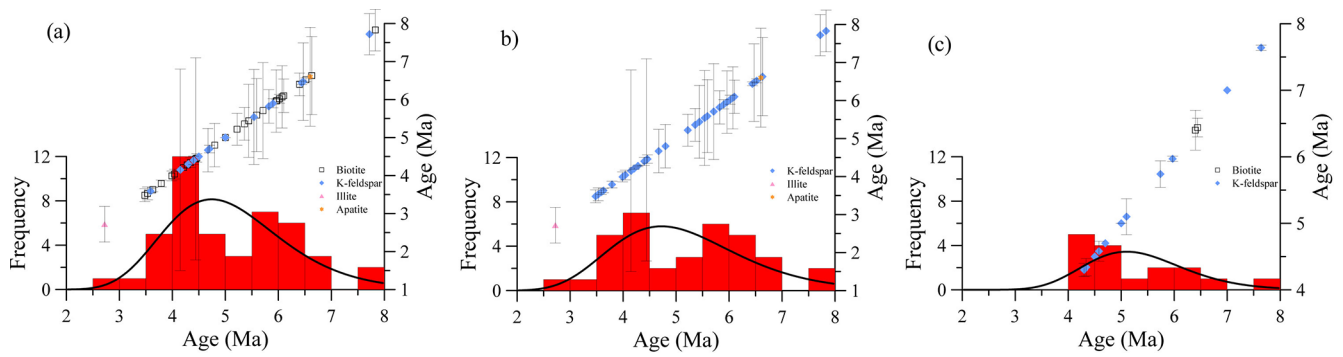
Figure 5. Frequency of thermochronological data from **(a)** the eastern and southern margin of DCS, **(b)** the eastern margin of DCS, and **(c)** the southern margin of DCS (data from references in Table S2).
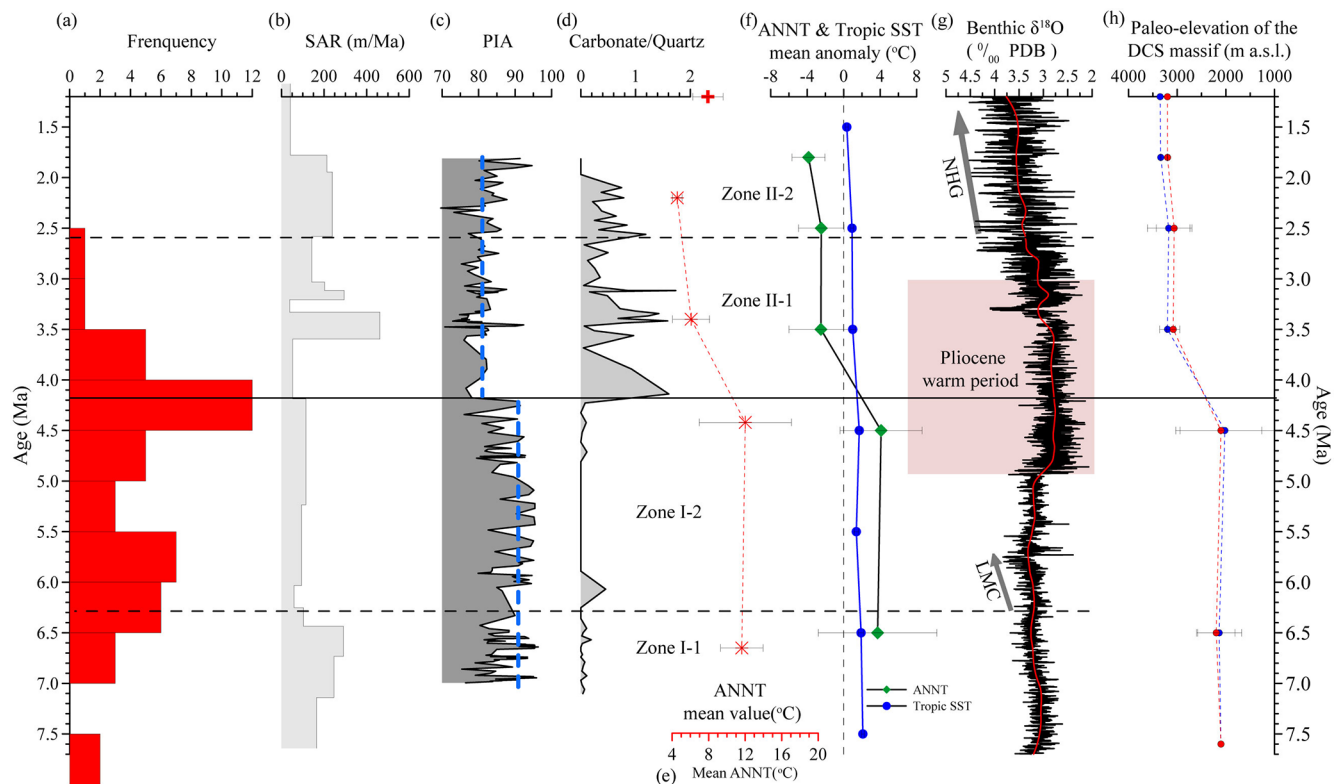
Figure 6. Comparison of **(a)** the frequency of thermochronological data from the eastern and southern margin of the DCS massif (data from references in Table S2), **(b)** the sediment accumulation rate (SAR), **(c)** the plagioclase index of alteration (PIA), **(d)** the ratio of carbonate / quartz (from C. X. Zhang et al., 2020), **(e)** the mean ANNT value of different zones, **(f)** the ANNT mean anomaly per Ma for the Dasongping section and the tropical sea-surface temperature (SST) mean anomaly per Ma since the Late Miocene (data from Herbert et al., 2016), **(g)** the marine benthic $\delta^{18}O$ stack (Westerhold et al., 2020) on the same timescale, and **(h)** the paleoelevation of the DCS massif (solid blue and red circles: the common temperature lapse rate of 5 and 6 °C km^{-1}). LMC: Late Miocene Cooling. NHG: Northern Hemisphere glaciation.

logical thermochronological data (Wang et al., 2020a), and the intensified normal fault activities at ∼ 3.6 and ∼ 2.7 Ma were further indicated by the late Neogene geochemical sedimentary record in the Dali Basin (C. X. Zhang et al., 2020). A significant provenance change in the infilling of sedimentary material in the Dali Basin occurred at ∼ 4.2 Ma (Fig. 6c

and d) (Li et al., 2014; C. X. Zhang et al., 2020), which is consistent with the age of the highest frequency in thermochronological data on time, ∼ 4.5–4.0 Ma (Fig. 5a). The highest mean SAR occurred at ∼ 3.6 Ma with the first occurrence of conglomerates in the Sanying Formation (Figs. 1c and 6b), which is consistent with the intensive thermochrono-

logical data $\sim$ 4.0–3.5 Ma (Figs. 5 and 6a). Similarities between the changes in Neogene sediment sequence and existing thermochronological data from the eastern and southern margin of DCS (Fig. 5) indicated that the DCS normal fault system was initiated at $\sim$ 7.6 Ma, intensified at $\sim$ 4.2 Ma, and enhanced at $\sim$ 3.6 and $\sim$ 2.7 Ma. The most recent tectonic activities in the DCS region have been dominated by differential uplift, which was likely caused by a combination of extension and isostatic adjustments resulting from climate change (Zhang et al., 2001; Wang et al., 2006).

4.2 Paleovegetation inferences based on palynological assemblages in the Dali Basin

A previous study showed that pollen grains of *Picea* and *Abies* are large and usually under-represented, whereas pollen grains of *Pinus* are usually over-represented (Erdtman, 1969). Only when its content exceeds 30 % can *Pinus* be considered to represent local sources (Li and Yao, 1990; Huang, 1993). As the main components of cold-temperature coniferous forests, *Picea* and *Abies* grow at relatively high altitudes of 3300–4200 m a.s.l. in the mountainous regions of southwestern China, and the percentages of *Picea* and *Abies* predominantly mirror their native habitats, regardless of any potential long-distance migration (Chen et al., 2014; Lu et al., 2008; Miao et al., 2022). *Quercus* evergreen types encompass alpine oaks, evergreen oaks, and Cyclobalanopsis plants, which are distributed across varying altitudes, resulting in their pollens having distinct climatic indications (Dai et al., 2018; Zhang et al., 2018). For instance, alpine oaks are predominantly found at altitudes ranging from 2500 to 3600 m a.s.l., dominating the high-altitude vegetation communities in the southeastern and southern regions of the Tibetan Plateau (X. Zhang et al., 2018, 2020). Therefore, when analyzing and discussing the climatic and ecological significance of the pollen of *Quercus* evergreen types, it is necessary to consider the changing characteristics of other pollen types within the pollen assemblage and to consider factors such as the corresponding altitude of the study area.

In the Dasongping section, broad-leaved tree pollen and herbaceous pollen are dominant in Zone I (0–510 m, $\sim$ 7.6–4.2 Ma), although small amounts of coniferous tree pollens, including *Picea*, *Tsuga*, and *Pinus*, are also present (Fig. 2). Compared to Zone I, coniferous pollens, including Pinaceae, *Pinus*, *Picea*, and *Abies*, are dominant in Zone II (510–1000 m, $\sim$ 4.2–1.8 Ma), whereas the percentages of *Tsuga* and broad-leaved trees are substantially lower (Fig. 2). This indicates that coniferous forests have been growing in the surrounding areas with altitudes of at least 3300 m a.s.l. since $\sim$ 4.2 Ma. Notably, *Quercus* evergreen types (*Quercus*E) are present throughout the Dasongping section, with a mean content of 19.0 % in Zone I and 3.7 % in Zone II, showing a significant negative correlation with that of coniferous pollens (Fig. 2). This indicates that *Quercus*E in the pollen assemblages is primarily composed of evergreen oak species

adapted to low-altitude, relatively warm environments. Otherwise, as the altitude of the region rises and the habitat of alpine oaks expands, their pollen content should also show an increasing trend, similar to that of conifers.

The dominant vegetation types were MTFO and WAMF at $\sim$ 7.6–6.3 Ma and WAMF at $\sim$ 4.8–4.2 Ma (Fig. 4a). The inferred vegetation types were similar to those of various adjacent basins. For example, vegetation in the Eryuan Basin comprised mainly mixed forest, suggestive of warm and humid conditions during the period 7.3–4.3 Ma (Wu et al., 2019). In the eastern Eryuan Basin, the main type of vegetation in the Lühe area was mixed forest of coniferous and broad-leaved trees during the Late Miocene (Xu et al., 2008). A mixed coniferous forest was also inferred from the Sanying Formation in the Lanping Basin and was considered to be of warm temperate affinity (Huang et al., 2020). COMX and CLEC were dominant at $\sim$ 4.2–1.8 Ma, with the exception of WAMF at $\sim$ 4.2–2.6 Ma (Fig. 4a). Previous studies have shown that the Eryuan palynoflora during the late Pliocene contained abundant *Pinus* with some *Quercus* and *Alnus* accompanied by herbs such as *Artemisia* and *Chenopodiaceae*, suggesting that the late Pliocene Eryuan vegetation was vertically zoned and included humid evergreen broad-leaved forest, needle and broad-leaved mixed evergreen forest, and coniferous forest (Tao and Kong, 1973; Kou et al., 2006; Wu et al., 2019). These results indicate that the vegetation in the Dali Basin has been characterized by vertical zonation since the Pliocene.

4.3 Climate change during the Late Miocene to Pleistocene in the Dali Basin

The Late Miocene was characterized by high chemical weathering intensity and much higher ANNT (Fig. 6c and e). The dominant vegetation types were MTFO and WAMF in the Dasongping section (Fig. 4a). A cooling episode during 6.2–5.2 Ma was identified from the geochemical record in the Zhaotong Basin (P. Li et al., 2020). However, no ANNT data were achieved during $\sim$ 6.3–5.0 Ma because of the sandstone lithology in the Dasongping section, whereas the plagioclase index of alteration (PIA) showed no particular change (Fig. 6c). The tropical SST data (Fig. 6f) and global marine δ^{18}O isotope records (Fig. 6g) (Zachos et al., 2001; Westerhold et al., 2020) showed that the Late Miocene to late Pliocene climate was relatively warm, except for a reduced zonal SST gradient that prevailed in the tropical Pacific Ocean during the Late Miocene (Late Miocene Cooling or LMC) (Herbert et al., 2016; Holbourn et al., 2018). Even the values of the ANNT mean anomaly ($\sim$ 3.9 °C) in the Dali Basin were much higher than those of the tropical SST mean anomaly ($\sim$ 1.8 °C); both of them showed very similar variation trends (Fig. 6f and g). The generally warm and humid climatic conditions in the Dali Basin during $\sim$ 7.6–4.2 Ma almost coincided with global climatic conditions.

The higher carbonate (calcite and dolomite) contents with less quartz and much lower values of PIA during the period ∼ 4.2–1.8 Ma (Fig. 6c and d) were consistent with the filling by detrital erosion material from bedrock surrounding DCS (C. X. Zhang et al., 2020). The ANNT showed the maximum decrease of ∼ 10 °C during ∼ 4.2–3.6 Ma and then stayed at ∼ 4 °C during the period of ∼ 2.6–1.8 Ma (Fig. 6b and e). The ANNT mean anomaly reduced from 4.1 to −2.5 °C in the Dali Basin and from 1.7 to 1.0 °C in the SST mean anomaly (Herbert et al., 2016; Holbourn et al., 2018) (Fig. 6f), which indicated that the temperature drop in the Dali Basin was significantly higher compared to in the tropical SST during ∼ 4.2–3.6 Ma. Noticeable, the Pliocene (∼ 5–3 Ma) was a stable and lasting warm period (Burke et al., 2018). This remarkable ANNT reduction in the Dali Basin during the period was in contradiction with the global warm Pliocene climate.

Both ANNT anomaly data and tropical SST anomaly data showed a continuous decrease since ∼ 2.7 Ma (Herbert et al., 2016; Holbourn et al., 2018); there had been little difference in the magnitude of temperature mean anomaly decrease between them (Fig. 6f). Global climate underwent a major reorganization, marked by a considerable intensification of the Northern Hemisphere glaciation (NHG) at ∼ 2.75 Ma (Prell and Kutzbach, 1992; Kleiven et al., 2002; Sigman et al., 2004), changing from the Pliocene warm climate stage into cold conditions (Zachos et al., 2001; Ravelo et al., 2004; Westerhold et al., 2020). The cold climate changes in the Dali Basin were almost consistent with the variation in global temperature since ∼ 2.7 Ma.

The climatic conditions in the Dali Basin were warm and humid from ∼ 7.6–4.2 Ma, cooler and humid from ∼ 4.2–3.6 Ma, and then cold and humid from ∼ 2.7–1.8 Ma. The remarkable ANNT reduction in the Dali Basin during the period of ∼ 4.2–3.6 Ma was in contradiction with the global warm Pliocene climate. Both the provenance changes at ∼ 4.2 Ma and the first occurrence of conglomerates in the Sanying Formation at ∼ 3.6 Ma in the Dali Basin (Figs. 1c and 6b, d) indicated a significant topographic growth of the northern segment of DCS during the period of ∼ 4.2–3.6 Ma (Li et al., 2013; C. X. Zhang et al., 2020). The previous climatic reconstruction results for the late Pliocene indicate that the climate conditions in western Yunnan during that period were still slightly warmer and wetter than they are now (Xie et al., 2012; Yao et al., 2012; Su et al., 2013). Given the absence of any pronounced cooling in global surface temperatures (Fig. 6g), we propose that this significant temperature decrease in the Dali Basin was primarily caused by the rapid topographic uplift of DCS during this period due to intense tectonic activities, as discussed in Sect. 4.1.

5 Constraints on the topography elevation of DCS during the Late Miocene to Pleistocene

Integrating results of tectonic activities surrounding DCS and climatic changes in the Dali Basin, the topography elevation of DCS during the Late Miocene to Pleistocene was discussed as follows.

5.1 Stage I (∼ 7.6–5.0 Ma): relatively low DCS

The paleotopography of DCS (especially in the northern segment) during ∼ 7.6–5.0 Ma was quantitatively reconstructed as ∼ 2100–2200 m a.s.l. based on the quantitative differences in ANNT values (Fig. 6f and h). At ∼ 8.0–7.6 Ma, the normal fault system initiated and the Dali Basin began to accumulate (Li et al., 2013; Wang et al., 2020a), and the sedimentary environment and provenance were stable during ∼ 7.6–4.2 Ma (Li et al., 2013; C. X. Zhang et al., 2020). Thermochronology research showed that a nearly isothermal phase until ∼ 5.0 Ma corresponded to a period during which the geothermal flux remained essentially constant and no significant unroofing occurred in the southern segment of DCS (Leloup et al., 1993; Li et al., 2012). The above information, together with the presence of lake and/or swamp facies sediments in the Dasongping section (Fig. 1c), implies that, during ∼ 7.6–5.0 Ma, the Dali Basin environment was characterized by a lake and/or swamp surrounded with forest of MTFO/WAMF types at low elevations (<∼ 2200 m a.s.l.) under warm and humid climatic conditions with an absence of significant tectonic activity during this period (Fig. 6a).

Therefore, we tentatively conclude that the paleoelevation of DCS likely exceeded 2000 m (may have reached up to ∼ 2200 m) above sea level at ∼ 7.6 Ma, which was consistent with the present average elevation (∼ 2200 m a.s.l.) of the surrounding region in the Dali Basin. Then, DCS maintained tectonic stability and relatively warm and humid climatic conditions during ∼ 7.6–5.0 Ma.

5.2 Stage II (∼ 5.0–3.5 Ma): rapid topographic growth of DCS

The existing thermochronological data were mainly concentrated during the period of ∼ 5.0–3.0 Ma (Fig. 5). This period had been promoted as a crucial time for the topographic formation of DCS (Leloup et al., 1993; Wang et al., 2006; Li et al., 2012). The reconstructed paleoelevation of the northern segment of DCS during ∼ 4.2–3.6 Ma changed from ∼ 2100–2200 to ∼ 3100–3350 m a.s.l. (Fig. 6h). Leloup et al. (1993) suggested that the normal fault of DCS initiated at ∼ 4.7 Ma and that the southern segment of DCS had been uplifted by at least 4000 m a.s.l. since the deposition began in Erhai. However, the age of older sediments in the Erhai Basin is still not precisely known (Guo et al., 1984). As discussed in Stage I, the paleoelevation of the northern segment of DCS likely exceeded 2000 m a.s.l. since the onset

of normal faulting of DCS at $\sim$ 7.6 Ma. Considering average elevation of 2200 m a.s.l. in the surrounding region and 4000 m a.s.l. in the southern part of DCS at present, it can be estimated that the southern segment of DCS may have risen by at most $\sim$ 2000 m rather than 4000 m. Based on the significant growth of $\sim$ 1000 m between $\sim$ 4.2 and $\sim$ 3.6 Ma, we calculated an uplift rate of at least $\sim$ 1.7 mm yr^{-1}. This rate was similar to the uplift rate of $\sim$ 2 mm yr^{-1} estimated by Leloup et al. (1993) and the rate of active normal faulting estimated by Allen et al. (1984).

The existing thermochronological data indicate high-frequency periods at $\sim$ 5.0–4.0 Ma in the southern segment and at $\sim$ 4.5–3.5 Ma in the eastern and northern segments of DCS, respectively (Fig. 5b and c). These data suggest that the intensified normal fault activities in the southern segment occurred earlier than those in the northern segment of DCS, which was also consistent with the roughly northward propagation indicated by the existing chronological data from the SEMTP (Wang et al., 2022). DCS may have risen by at least $\sim$ 1000 m in the northern segment and at most $\sim$ 2000 m in the southern segment. Therefore, we propose that DCS may have reached 3100–3350 m a.s.l. in the north at $\sim$ 3.5 Ma and $\sim$ 4000 m a.s.l. in the south at $\sim$ 4.7 Ma. Coniferous pollens, including *Pinus*, *Tsuga*, *Picea*, and *Abies*, are present throughout the Dasongping section, especially in Zone II (4.2–1.8 Ma) (Fig. 2). These findings indicate that significant vertical climatic zoning of vegetation on DCS may have formed since $\sim$ 4.7–4.2 Ma, which was consistent with the Pliocene Eryuan vertically zoned vegetation (Tao and Kong, 1973; Kou et al., 2006; Wu et al., 2019).

5.3 Stage III ($\sim$ 3.5–1.8 Ma): intense erosion of DCS

Taking into account the ongoing global cooling, the paleotopography of the northern segment of DCS during this period was quantitatively reconstructed as $\sim$ 3200–3350 m a.s.l. (Fig. 6h). As discussed in Stage II, the paleoelevation of the southern part of DCS had possibly already reached $\sim$ 4000 m a.s.l. Today, the average elevations of the northern and southern segments of DCS are 3500 and 4000 m, respectively. During the period of 3.5–1.8 Ma, only a few low-temperature thermochronological data were available along the eastern margin of DCS, while no data were recorded in the southern margin (Figs. 5 and 6a), indicating weak tectonic activity during this time, especially in the southern segment of DCS. Compared to the vertical distribution of modern vegetation (Fig. 3), the dominant vegetation of CLEC and COMX during the period of 3.5–1.8 Ma (Fig. 6a) indicates that DCS may have reached its current elevation after $\sim$ 1.8 Ma, undergoing topographic uplifts of $\sim$ 150–300 m in the northern segment of DCS.

Today, there is a very flat surface on the top of DCS, which can be traced for 100 km from the northern edge to the southern edge of the massif. The existence of a relict surface on the top of DCS suggests that DCS was not subject to un-

roofing during the Late Cenozoic (Fan et al., 2006; Wang et al., 2006). The dominant sedimentation facies were alluvial facie, with a high SAR between $\sim$ 3.5 and 2.7 Ma, and foothill pluvial facie, which became dominant between $\sim$ 2.7 and 1.8 Ma, with a much higher mean SAR (Figs. 1c and 6a, b). Syntectonic sediments with massive conglomerates developed in the upper $\sim$ 200 m of the Dasongping section (Fig. 1c). These discrepancies between sediment sequence and thermochronological data suggest that the intensification of SARs was likely caused by intense erosion related to climate cooling. Therefore, we propose that the ongoing global climate cooling, along with the initiation and development of the NHG, played a key role in maintaining the cold and humid climate monsoon conditions in the Dali Basin. This possibly resulted in an intense erosion of DCS since 2.7 Ma, ultimately leading to the high SAR in the Dali Basin and the accumulation of $\sim$ 2200 m thick sediments in Erhai.

In conclusion, DCS may have reached a paleoelevation of at least $\sim$ 2000 m a.s.l. at $\sim$ 7.6 Ma and maintained tectonic stability during $\sim$ 7.6–5.0 Ma. Subsequently, significant uplift of $\sim$ 1000 m occurred between $\sim$ 5.0 and $\sim$ 3.5 Ma in the northern segment of DCS, followed by slow growth during $\sim$ 3.5–1.8 Ma. Finally, the northern segment of DCS reached an elevation of 3500 m a.s.l. after $\sim$ 1.8 Ma. Significant changes in vegetation in the Dali Basin since the Late Miocene were primarily due to a marked increase in the paleoelevation of DCS. Ongoing global cooling and the associated development of the NHG played a significant role in maintaining cold climatic conditions in the Dali Basin, resulting in intense erosion of DCS since $\sim$ 2.7 Ma. Our findings suggest that quantitative paleotemperature reconstruction based on terrestrial pollen assemblages, combined with geochronological, thermochronological, and sedimentary data, can provide direct constraints on the paleotopographic evolution of mountains.

Author contributions. CZ and HW designed the study. CZ carried out data preparation. XZ and YD conducted pollen analyses. YJ and WZ conducted climate reconstruction analyses. CZ generated the figures. CZ, HW, SL, and CD contributed to the writing of the article.

References

Allen, C. R., Gillespie, A. R., Han, Y., Sieh, K. E., Zhang, B., and Zhu, C.: Red River and associated faults, Yunnan province, China: Quaternary geology, slip rates, and seismic hazard, Geol. Soc. Am. Bull., 95, 686–700, https://doi.org/10.1130/0016-7606(1984)95<686:RRAAFY>2.0.CO;2, 1984.

Burke, K. D., Williams, J. W., Chandler, M. A., Haywood, A. M., Lunt, D. J., and Otto-Bliesner, B. L.: Pliocene and Eocene provide best analogs for near-future climates, P. Natl. Acad. Sci. USA, 115, 13288–13293, https://doi.org/10.1073/pnas.1809600115, 2018.

Cao, K., Leloup, P. H., Wang, G., Liu, W., Mahéo, G., Shen, T., Xu, Y., Sorrel, P., and Zhang, K.: Thrusting, exhumation, and basin fill on the western margin of the South China block during the India-Asia collision, GSA Bull., 133, 74–90, https://doi.org/10.1130/b35349.1, 2021.

Cao, S. Y., Neubauer, F., Liu, J. L., Genser, J., and Leiss, B.: Exhumation of the Diancang Shan metamorphic complex along the Ailao Shan-Red River belt, southwestern Yunnan, China: Evidence from ^{40}Ar/^{39}Ar thermochronology, J. Asian Earth Sci., 42, 525–550, https://doi.org/10.1016/j.jseaes.2011.04.017, 2011.

Chen, F. H., Chen, X. M., Chen, J. H., Zhou, A., Wu, D., Tang, L. Y., Zhang, X. J., Huang, X. Z., and Yu, J. Q.: Holocene vegetation history, precipitation changes and Indian Summer Monsoon evolution documented from sediments of Xingyun Lake, southwest China, J. Quaternary Sci., 29, 661–674, https://doi.org/10.1002/jqs.2735, 2014.

Chen, Z. Y.: The Climate of Yunnan, China Meteorological Press, Beijing, China, 1–196, ISBn 7502932356, 2001.

Clark, M. K. and Royden, L. H.: Topographic Ooze: Building the Eastern Margin of Tibet by Lower Crustal Flow, Geology, 28, 703–706, https://doi.org/10.1130/0091-7613(2000)28<703:TOBTEM>2.0.CO;2, 2000.

Clark, M. K., Schoenbohm, L. M., Royden, L. H., Whipple, K. X., Burchfiel, B. C., Zhang, X., Tang, W., Wang, E., and Chen, L.: Surface uplift, tectonics, and erosion of eastern Tibet from large-scale drainage patterns, Tectonics, 23, TC1006, https://doi.org/10.1029/2002TC001402, 2004.

Clark, M. K., House, M. A., Royden, L. H., Whipple, K. X., Burchfiel, B. C., Zhang, X., and Tang, W.: Late Cenozoic uplift of southeastern Tibet, Geology, 33, 525–528, https://doi.org/10.1130/G21265.1, 2005.

Dai, L., Hao, Q., and Mao, L.: Morphological diversity of Quercus fossil pollen in the northern South China Sea during the last glacial maximum and its paleoclimatic implication, PLoS ONE, 13, e0205246, https://doi.org/10.1371/journal.pone.0205246, 2018.

Dupont-Nivet, G., Hoorn, C., and Konert, M.: Tibetan uplift prior to the Eocene-Oligocene climate transition: Evidence from pollen analysis of the Xining Basin, Geology, 36, 987, https://doi.org/10.1130/G25063A.1, 2008.

Erdtman, G.: Handbook of Palynology-An introduction to the stydy of Pollen Grains and Spores, Munksgaard, Copenhagen, 1–466, https://doi.org/10.1002/fedr.19710810815, 1969.

Fan, C., Wang, G., Wang, S. F., and Wang, E.: Structural interpretation of extensional deformation along the Dali fault system, southeastern margin of the Tibetan plateau, Int. Geol. Rev., 48, 287–310, https://doi.org/10.2747/0020-6814.48.4.287, 2006.

Fick, S. E. and Hijmans, R. J.: WorldClim 2: new 1-km spatial resolution climate surfaces for global land areas, Int. J. Climatol., 37, 4302–4315, https://doi.org/10.1002/joc.5086, 2017.

Gourbet, L., Leloup, P. H., Paquette, J.-L., Sorrel, P., Maheo, G., Wang, G. C., Xu, Y. D., Cao, K., Antoine, P.-O., Eymard, I., Liu, W., Lu, H. J., Replumaz, A., Chevalier, M.-L., Zhang, K. X., Wu, J., and Shen, T. Y.: Reappraisal of the Jianchuan Cenozoic basin stratigraphy and its implications on the SE Tibetan plateau evolution, Tectonophysics, 700–701, 162–179, https://doi.org/10.1016/j.tecto.2017.02.007, 2017.

Guo, S. M., Zhang, J., Li, X. G., Xiang, H. F., Chen, T. N., and Zhang, G. W.: Fault displacement and recurrence intervals of earthquakes at the northern segment of the Honghe fault zone, Yunnan Province, Seismol. Geol., 6, 77–91, 1984.

Han, S. Q., Chen, Q. L., and Zhang, Y. S.: K-Ar age of authigenic illite in fault gouge in the northern section of Red River fault and geological significance, Quatern. Sci., 27, 1129–1130, 2011.

Harrison, T. M., Gopeland, P., Kidd, W. S. F., and Lovera, O. M.: Activation of the Nyainqentanghla Shear Zone: Implications for uplift of the southern Tibetan Plateau, Tectonics, 14, 658–676, https://doi.org/10.1029/95TC00608, 1995.

Herbert, T. D., Lawrence, K. T., Tzanova, A., Peterson, L. C., Caballero-Gill, R., and Kelly, C. S.: Late Miocene global cooling and the rise of modern ecosystems, Nat. Geosci., 9, 843–849, https://doi.org/10.1038/ngeo2813, 2016.

Herman, F., Seward, D., Valla, P., Carter, A., Kohn, B., Willett, S. D., and Ehlers, T. A.: Worldwide acceleration of mountain erosion under a cooling climate, Nature, 504, 423–426, https://doi.org/10.1038/nature12877, 2013.

Hoke, G. D., Liu-Zeng, J., Hren, M. T., Wissink, G. K., and Garzione, C. N.: Stable isotopes reveal high southeast Tibetan Plateau margin since the Paleogene, Earth Planet Sc. Lett., 394, 270–278, https://doi.org/10.1016/j.epsl.2014.03.007, 2014.

Holbourn, A. E., Kuhnt, W., Clemens, S. C., Kochhann, K. G. D., Jöhnck, J., Lübbers, J., and Anderson, N.: Late Miocene climate cooling and intensification of southeast Asian winter monsoon, Nat. Commun., 9, 1584, https://doi.org/10.1038/s41467-018-03950-1, 2018.

Houseman, G. and England, P.: Crustal thickening versus lateral expulsion in the Indian-Asian continental collision, J. Geophys. Res., 98, 12233–12249, https://doi.org/10.1029/93JB00443, 1993.

Huang, C. Y.: A study on pollen in surface soil from the western Xizang, Arid Land Geogr., 16, 75–83,1993.

Huang, Y. J., Gao, S. J., Tang, F. J., Meng, Q., Q., and An, C. R.: A warm-temperate forest of mixed coniferous type from the upper Pliocene Sanying Formation (southeastern edge of Tibetan Plateau) and its implications for palaeoecology and palaeoaltimetry, Palaeogeogr. Palaeocl. Palaeoecol., 538, 109486, https://doi.org/10.1016/j.palaeo.2019.109486, 2020.

Kleiven, H. F., Jansen, E., Fronval, T., and Smith, T. M.: Intensification of Northern Hemisphere glaciations in the circum Atlantic region (3.5–2.4 Ma) ice rafted detritus evidence, Palaeogeogr. Palaeocl. Palaeoecol., 184, 213–223, https://doi.org/10.1016/S0031-0182(01)00407-2, 2002.

Kou, X. Y., Ferguson, D. K., Xu, J. X., Wang, Y. F., and Li, C. S.: The reconstruction of paleovegetation and paleoclimate in the late Pliocene of west Yunnan, China, Climatic Change, 77, 431–448, https://doi.org/10.1007/s10584-005-9039-5, 2006.

Leloup, P. H., Harrison, T. M., Ryerson, F. J., Chen, W. J., Li, Q., Tapponnier, P., and Lacassin, R.: Structural, petrological and thermal evolution of a tertiary ductile strike-slip shear zone, Diancong shan, Yunnan, J. Geophys. Res., 98, 6715–6743, https://doi.org/10.1029/92JB02791, 1993.

Leloup, P. H., Lacassin, R., Tapponnier, P., Schärer, U., Zhong, D. L., Liu, X. H., Zhang, L. S., Ji, S. C., and Trinh, P. T.: The Ailao Shan-Red River shear zone (Yunnan, China) Tertiary transform bounday of Indochina, Tectonophysics, 251, 3–84, https://doi.org/10.1016/0040-1951(95)00070-4, 1995.

Li, B. L., Ji, J. Q., Lo, C. H., Gong, J. F., and Qing, J. C.: The structural style and timing of uplift of the Ailao Shan- Diancang Range, West Yunnan, China, Seismol. Geol., 34, 696–712, 2012.

Li, P., Zhang, C. X., Kelley, J., Deng, C. L., Ji, X. P., Jablonski, N. G., Wu, H. B., Fu, Y., Guo, Z. T., and Zhu, R. X.: Late Miocene Climate Cooling Contributed to the Disappearance of Hominoids in Yunnan Region, Southwestern China, Geophys. Res. Lett., 47, e2020GL087741, https://doi.org/10.1029/2020GL087741, 2020.

Li, S. H., Deng, C. L., Yao, H. T., Huang, S., Liu, C. Y., He, H. Y., Pan, Y. X., and Zhu, R. X.: Magnetostratigraphy of the Dali Basin in Yunnan and implications for late Neogene rotation of the southeast margin of the Tibetan Plateau, J. Geophys. Res., 118, 791–807, https://doi.org/10.1002/jgrb.50129, 2013.

Li, S. H., Deng, C. L., Paterson, G. A., Yao, H. T., Huang, S., Liu, C. Y., He, H. Y., Pan, Y. X., and Zhu, R. X.: Tectonic and sedimentary evolution of the late Miocene-Pleistocene Dali Basin in the southeast margin of the Tibetan Plateau: evidences from anisotropy of magnetic susceptibility and rock magnetic data, Tectonophysics, 629, 362–377, https://doi.org/10.1016/j.tecto.2014.05.035, 2014.

Li, S. H., Su, T., Spicer, R. A., Xu, C. L., Sherlock, S., Halton, A., Gregory, H., Tian, Y. M., Zhang, S. T., Zhou, Z. K., Deng, C. L., and Zhu, R. X.: Oligocene deformation of the Chuandian terrane in the SE margin of the Tibetan Plateau related to the extrusion of Indochina, Tectonics, 39, e05974, https://doi.org/10.1029/2019TC005974, 2020.

Li, W. Y. and Yao, Z. J.: A study on the quantitative relationship between *Pinus* pollen in surface sample and *Pinus* vegetation, Acta Bot. Sin., 32, 943–950, 1990.

Liu, J., Tang, L., Qiao, Y., Head, M. J., and Walker, D.: Late Quaternary vegetation history at Menghai, Yunnan province, southwest China, J. Biogeogr., 13, 399–418, https://doi.org/10.2307/2844965, 1986.

Lu, H. Y., Wu, N. Q., Yang, X. D., Shen, C. M., Zhu, L. P., Wang, L., Li, Q., Xu, D. K. Tong, G. B., and Sun, X. J.: Spatial pattern of *Abies* and *Picea* surface pollen distribution along the elevation gradient in the Qinghai–Tibetan Plateau and Xinjiang, China, Boreas, 37, 254–262, https://doi.org/10.1111/j.1502-3885.2007.00019.x, 2008.

Miao, Y. F., Fang, X. M., Sun, J. M., Xiao, W. J., Yang, Y. H., Wang, X. L., Farnsworth, A., Huang, K. Y., Ren, Y. L., Wu, F. L., Qiao, Q. Q., Zhang, W. L., Meng, Q. Q., Yan, X. L., Zheng, Z., Song, C. H., and Utescher, T.: A new biologic paleoaltimetry indicating Late Miocene rapid uplift of northern Tibet Plateau, Science, 378, 1074–4079, https://doi.org/10.1126/science.abo2475, 2022.

Ming, T. L. and Fang, R. Z.: The vegetation on Cangshan Yunnan and the distribution of genus Rhododendron (in Chinese with English abstract), Acta Bot. Yunan., 4, 383–391, 1982.

Prell, W. L. and Kutzbach, J. E.: Sensitivity of the Indian monsoon to forcing parameters and implications for its evolution, Nature, 360, 647–652, https://doi.org/10.1038/360647a0, 1992.

Prentice, C. I., Guiot, J., Huntley, B. D. J., and Cheddadi, R.: Reconstructing biomes from palaeoecological data: a general method and its application to European pollen data at 0 and 6 ka, Clim. Dynam., 12, 185–194, https://doi.org/10.1007/BF00211617, 1996.

Ravelo, A. C., Andreasen, D. H., Lyle, M., Lyle, A. O., and Wara, M.: Regional climate shifts caused by gradual global cooling in the Pliocene epoch, Nature, 429, 263–267, https://doi.org/10.1038/nature02567, 2004.

R Core Team: R software version 4.3.3, https://www.r-project.org/ (last access: 31 October 2024), 2024.

Reiners, P. W. and Brandon, M. T.: Using thernochronology to understand orogenic erosion, Annu. Rev. Earth Plant. Sci., 34, 419–466, https://doi.org/10.1146/annurev.earth.34.031405.125202, 2006.

Schildgen, T. F., van der Beek, P. A., Sinclair, H. D., and Thiede, R. C.: Spatial correlation bias in late-Cenozoic erosion histories derived from thermochronology, Nature, 559, 89–93, https://doi.org/10.1038/s41586-018-0260-6, 2018.

Shen, J., Jones, R. T., Yang, X. D., Dearing, J. A., and Wang, S. M.: The Holocene vegetation history of Lake Erhai, Yunnan province southwestern China: the role of climate and human forcings, Holocene, 16, 265–276, https://doi.org/10.1016/j.atmosenv.2006.12.038, 2006.

Sigman, D. M., Jaccard, S. L., and Haug, G. H.: Polar ocean stratification in a cold climate, Nature, 428, 59–63, https://doi.org/10.1038/nature02357, 2004.

Song, X. Y., Spicer, R. A., Yang, J., Yao, Y. F., and Li, C. S.: Pollen evidence for an Eocene to Miocene elevation of central southern Tibet predating the rise of the High

Himalaya, Palaeogeogr. Palaeocl. Palaeoecol., 297, 159–168, https://doi.org/10.1016/j.palaeo.2010.07.025, 2010.

Su, T., Jacques, F. M. B., Spicer, R. A., Liu, Y.-S., Huang, Y.-J., Xing, Y.-W., and Zhou, Z.-K.: Post-Pliocene establishment of the present monsoonal climate in SW hina: evidence from the late Pliocene Longmen megaflora, Clim. Past, 9, 1911–1920, https://doi.org/10.5194/cp-9-1911-2013, 2013.

Su, T., Spicer, R. A., Li, S. H., Xu, H., Huang, J., Sherlock, S., Huang, Y. J., Li, S. F., Wang, L., Jia, L. B., Deng, W. Y. D., Liu, J., Deng, C. L., Zhang, S. T., Valdes, P. J., and Zhou, Z. K.: Uplift, climate and biotic changes at the Eocene-Oligocene transition in south-eastern Tibet, Natl. Sci. Rev., 6, 495–504, https://doi.org/10.1093/nsr/nwy062, 2019.

Sun, A. Z., Luo, Y. L., Wu, H. B., Chen, X. D., Li, Q., Yu, Y. Y., Sun, X. J., and Guo, Z. T.: An updated biomization scheme and vegetation reconstruction based on a synthesis of modern and mid-Holocene pollen data in China, Global Planet. Change, 192, 103178, https://doi.org/10.1016/j.gloplacha.2020.103178, 2020.

Sun, J. M., Xu, Q. H., Liu, W. M., Zhang, Z. Q., Xue, L., and Zhao, P.: Palynological evidence for the latest Oligocene-early Miocene paleoelevation estimate in the Lunpola Basin, central Tibet, Palaeogeogr. Palaeocl. Palaeoecol., 399, 21–30, https://doi.org/10.1016/j.palaeo.2014.02.004, 2014.

Tang, M. Y., Liu-Zeng, J., Hoke, G. D., Xu, Q., Wang, W. T., Li, Z. F., Zhang, J. Y., and Wang, W.: Paleoelevation reconstruction of the Paleocene-Eocene Gonjo basin, SE-central Tibet, Tectonophysics, 712–713, 170–181, https://doi.org/10.1016/j.tecto.2017.05.018, 2017.

Tang, Y., Liu, J. L., Tran, M. D., Song, Z. J., Wu, W. B., Zhang, Z. C., Zhao, Z. D., and Chen, W.: Timing of left-lateral shearing along the Ailao Shan-Red River shear zone: Constraints from zircon U-Pb ages from granitic rocks in the shear zone along the Ailao Shan Range, Western Yunnan, China, Int. J. Earth Sci.-Geol. Rund., 102, 605–626, https://doi.org/10.1007/s00531-012-0831-y, 2013.

Tao, J. R. and Kong, Z. C.: The forssil florule and sporo-pollen assemblage of the Shang-in coal series of Eryuan, Yunnan, Acta Bot. Sin., 15, 120–126, 1973.

Tapponnier, P., Lacassin, R., Leloup, P. H., Schärer, U., Zhong, D. L., Wu, H. W., Liu, X. H., Ji, S. C., Zhang, L. S., and Zhong, J. Y.: The Ailao Shan/Red River metamorphic belt: Tertiary left-lateral shear between Indochina and South China, Nature, 343, 431–437, https://doi.org/10.1038/343431a0, 1990.

Wang, E., Burchfiel, B. C., Royden, L. H., Chen, L. Z., Chen, J. S., Li, W. X., and Chen, Z. L.: Late Cenozoic Xianshuihe-Xiaojiang, Red River, and Dali fault systems of Southwestern Sichuan and Central Yunnan, China, Geol. Soc. Am. Spec. Pap., 327, 1–108, https://doi.org/10.1130/0-8137-2327-2.1, 1998.

Wang, E., Fan, C., Wang, G., Shi, X. H., Chen, L. Z., and Chen, Z. L.: Defomational and geonorphic processes in the formation of the AIlao Shan- Diancang Rang, West Yunnan, Quatern. Sci., 26, 220–227, 2006.

Wang, Y., Wang, Y. J., Schoenbohm, L. M., Zhang, P. Z., B., Z., Sobel, E. R., Zhou, R. J., Shi, X. H., Zhang, J. J., Stockli, D. F., and Guo, X. F.: Cenozoic exhumation of the Ailaoshan-Red River shear zone: New insights from low-temperature thermochronology, Tectonics, 39, e06151, https://doi.org/10.1029/2020TC006151, 2020a.

Wang, Y., Wang, Y. J., Zhang, P. Z., Schoenbohm, L. M., Zhang, B., Zhang, J. J., Zhou, R. J., Stockli, D. F., Seagren, E. G., Wang, F., and Wu, L.: Intracontinental deformation within the India-Eurasia oblique convergence zone: Case studies on the Nantinghe and Dayingjiang faults, Geol. Soc. Am. Bull., 132, 850–862, https://doi.org/10.1130/B35338.1, 2020b.

Wang, Y., Wang, Y. J., Zhang, P. Z., Zhang, J. J., Zhang, B., Liu, J., Zhou, R. J., Wang, W. T., Zhang, H. P., and Li, C. J.: Cenozoic tectonic evolution of regional fault systems in the SE Tibetan Plateau, Sci. China Earth Sci., 65, 601–623, https://doi.org/10.1007/s11430-021-9880-3, 2022.

Westerhold, T., Marwan, N., Drury, A. J., Liebrand, D., Agnini, C., Anagnostou, E., Barnet, J. S. K., Bohaty, S. M., Vleeschouwer, D. D., Florindo, F., Frederichs, T., Hodell, D. A., Holbourn, A. E., Kroon, D., Lauretano, V., Littler, K., Lourens, L. J., Lyle, M., Pälike, H., Röhl, U., Tian, J., Wilkens, R. H., Wilson, P. A., and Zachos, J. C.: An astronomically dated record of Earth's climate and its predictability over the last 66 million years, Science, 369, 1383–1387, https://doi.org/10.1126/science.aba6853, 2020.

Wu, F. L., Gao, S. J., Tang, F. J., Meng, Q. Q., and An, C. R.: A late Miocene-early Pleistocene palynological record from the Yunnan Plateau and its climatic and tectonic implications for the Eryuan Basin, China, Palaeogeogr. Palaeocl. Palaeoecol., 530, 190–199, https://doi.org/10.1016/j.palaeo.2019.05.037, 2019.

Xiang, H. F., Wan, J. L., Han, Z. J., Guo, S. M., Zhang, W. X., Chen, L. C., and Dong, X. Q.: Geological analysis and FT dating of the large-scale right-lateral strike-slip movement of the Red River fault Zone, Sci. China Ser. D, 50, 331–342, https://doi.org/10.1007/s11430-007-2037-x, 2007.

Xie, S., Sun, B., Wu, J., and Lin, Z.: Palaeoclimatic estimates for the Late Pliocene based on leaf physiognomy from western Yunnan, China, Turk. J. Earth Sci., 21, 251–261, https://doi.org/10.3906/yer-1003-23, 2012.

Xu, J. X., Ferguson, D. K., Li, C. S., and Wang, Y. F.: Late Miocene vegetation and climate of the Lühe region in Yunnan, southwestern China, Rev. Palaeobot. Palynol., 148, 36–59, https://doi.org/10.1016/j.revpalbo.2007.08.004, 2008.

Yao, Y., Bruch, A. A., Cheng, Y. M., Mosbrugger, V., Wang, Y. F., and Li, C. S.: Monsoon versus uplift in Southwestern China-Late Pliocene climate in Yuanmou Basin, Yunnan, Plos One, 5, e37760, https://doi.org/10.1371/journal.pone.0037760, 2012.

Zhang, C. X.: Biome scores and annual mean temperature data of Dasongping section and Paleoelevation data of Diancang Shan, Science Data Bank [data set], https://doi.org/10.57760/sciencedb.18211, 2024.

Zhang, C. X., Li, S. H., Zhang, X. Y., Li, P., Deng, C. L., and Guo, Z. T.: A high-resolution Late Neogene geochemical record of the southeastern margin of the Tibetan Plateau: Constraints on Dali fault system activity and uplift of the Diancang Shan massif, J. Asian Earth Sci., 195, 104335, https://doi.org/10.1016/j.jseaes.2020.104335, 2020.

Zachos, J. C., Pagani, M., Sloan, L., Thomas, E., and Billups, K.: Trends, rhythms, and aberrations in global climate 65 Ma to present, Science, 292, 689–693, https://doi.org/10.1126/science.1059412, 2001.

Zhang, P. Z., Molnar, P., and Downs, W. R.: Increased sedimentation rates and grain sizes 2–4 Myr ago due to the influence of climate change on erosion rates, Nature, 410, 891–897, https://doi.org/10.1038/35073504, 2001.

Zhang, W. C., Wu, H. B., Cheng, J., Geng, J. Y., Li, Q., Sun, Y., Yu, Y. Y., Lu, H. Y., and Guo, Z. T.: Holocene seasonal temperature evolution and spatial variability over the Northern Hemisphere landmass, Nat. Commun., 13, 5334, https://doi.org/10.1038/s41467-022-33107-0, 2022a.

Zhang, W. C., Wu, H. B., Li, Q., Liu, Z. Y., and Cheng, J.: Large training dataset is crucial for analogue-based precipitation reconstruction during the early Holocene, Sci. Bull., 67, 1118–1121, https://doi.org/10.1016/j.scib.2022.03.007, 2022b.

Zhang, X., Huang, K. Y., Zheng, Z., Zhang, Y. Z., Wan, Q. C., and Tian, L. P.: Pollen morphology of *Quercus* sect. *Ilex* and its relevance for fossil pollen identification in southwest China, Grana, 57, 401–414, https://doi.org/10.1080/00173134.2018.1480653, 2018.

Zhang, X., Zheng, Z., Huang, K. Y., Yang, X. Q., and Tian, L. P.: Sensitivity of altitudinal vegetation in southwest China to changes in the Indian summer monsoon during the past 68 000 years, Quaternary Sci. Rev., 239, 106359, https://doi.org/10.1016/j.quascirev.2020.106359, 2020.